

Electronic Supplementary Information

Lightweight and Highly Bendable and Foldable Electrochromic Films Based on All-Solution-Processed Bilayer Nanowire Networks

Kerui Li^a, Qinghong Zhang^b, Hongzhi Wang^{a}, Yaogang Li^{b*}*

^a State Key Laboratory for Modification of Chemical Fibers and Polymer Materials,
College of Materials Science and Engineering, Donghua University, Shanghai 201620,
People's Republic of China.

^b Engineering Research Center of Advanced Glasses Manufacturing Technology,
Ministry of Education, Donghua University, Shanghai 201620, People's Republic of
China.

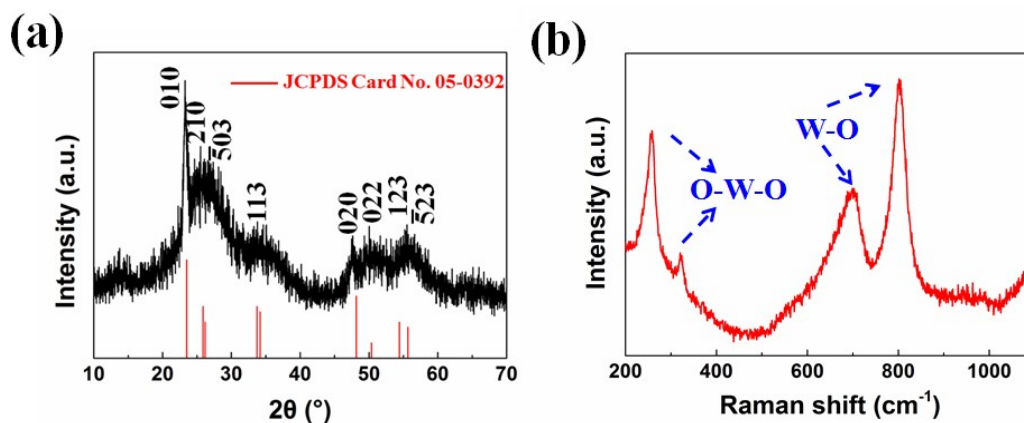


Figure S1. XRD (a) and the Raman (b) spectrum of the as-obtained $\text{W}_{18}\text{O}_{49}$ NWs.

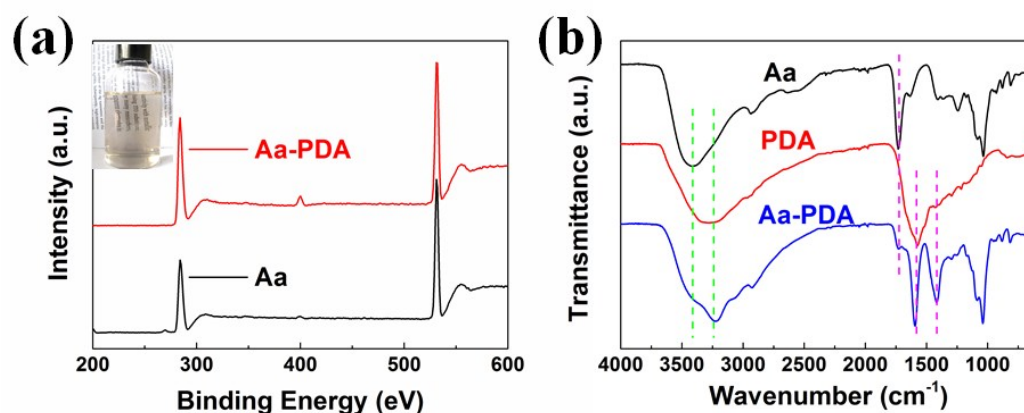


Figure S2. (a) XPS spectra of Aa-PDA (red line) and Aa (black line) (inset shows a digital photograph of the Aa-PDA solution in mixed solvent of water and ethanol with a volume ratio of 1:1); (b) FTIR spectra of Aa, PDA and Aa-PDA.

The spectrum of Aa displayed a broad absorption band around 3410 cm^{-1} , characteristic of the O–H stretching vibration. The peaks at ~ 1730 and $\sim 1035\text{ cm}^{-1}$ are characteristic of the C=O stretching vibration and the C–O–C asymmetric vibration, respectively. The spectrum of PDA displayed a peak at $\sim 1595\text{ cm}^{-1}$, characteristic of the stretching vibration of C=C and the deformation vibration of N–H, respectively. After complex formation, peaks at $\sim 1595\text{ cm}^{-1}$ and $\sim 1415\text{ cm}^{-1}$ were present, corresponding to COO^- (carboxylate) asymmetric and symmetric vibrations, respectively. These peaks resulted from the deprotonation of $-\text{COOH}$ in Aa by ammonia.

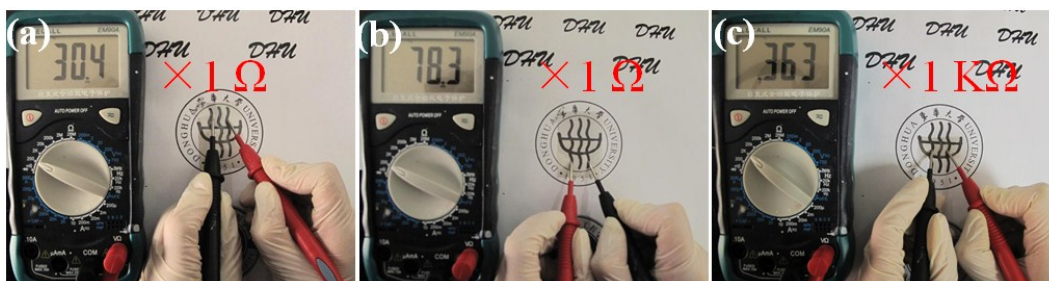


Figure S3. Resistance values of the AAF before (a) and after (b) being subjected to cyclic voltammetry for three cycles; (c) Resistance of the AAPF after the same treatment.

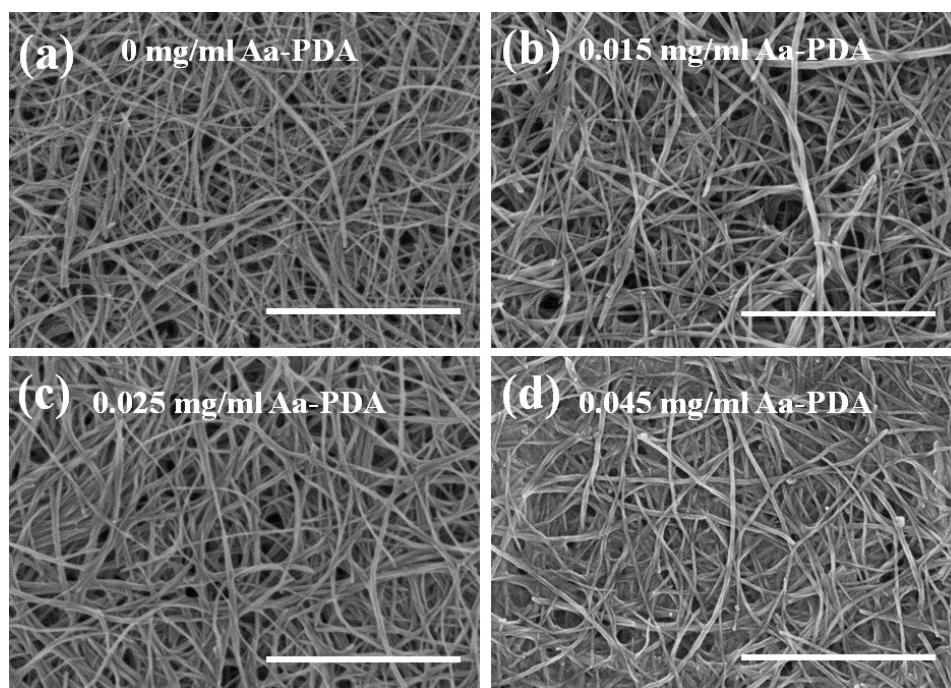


Figure S4. (a–d) FE-SEM images of EC layers prepared *via* spray-coating $W_{18}O_{49}$ NW dispersion with increasing concentrations of Aa-PDA. Scale bars: 1 μ m.

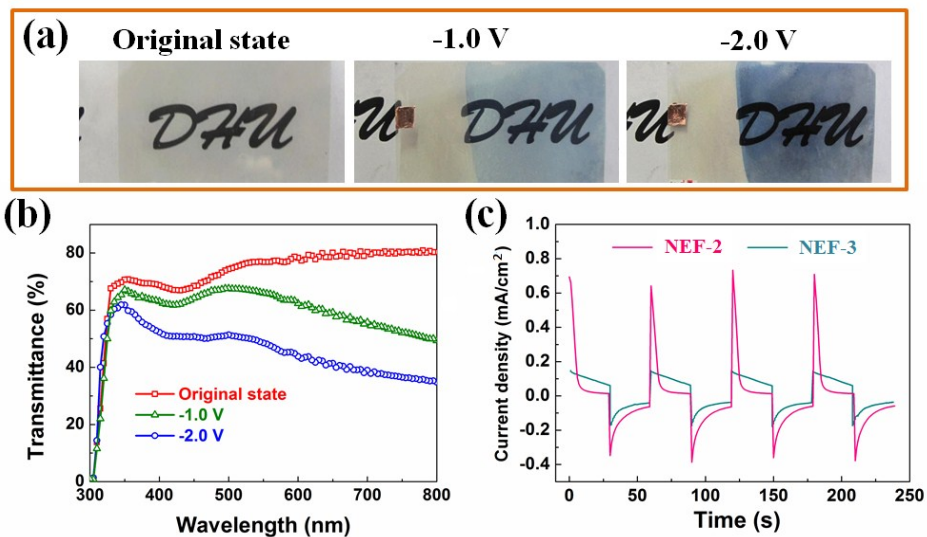


Figure S5. Digital photographs (a) and corresponding UV-vis transmittance spectra (b) of NEF-3 measured at original state, -1 V and -2 V, respectively; (c) The variation of the current density vs. time for NEF-2 and NEF-3 characterized by chronoamperometry using square potentials (between $+0.7$ and -1.0 V).

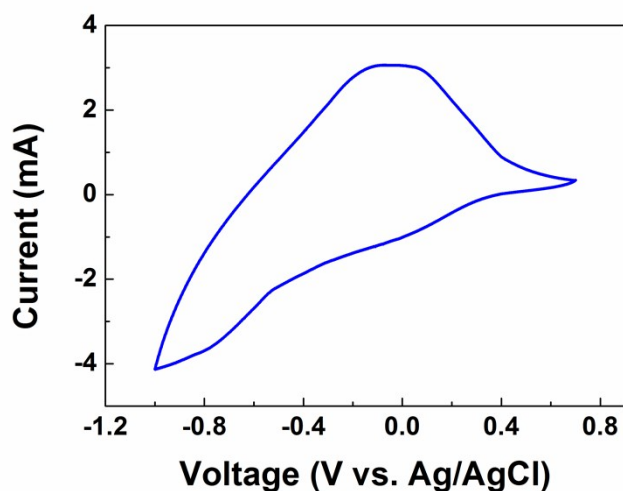


Figure S6. The CV curve of NEF-2 between -1.0 and 0.7 V at a scan rate of 50 mV/s in PC solution containing 1.0 M LiClO_4 .

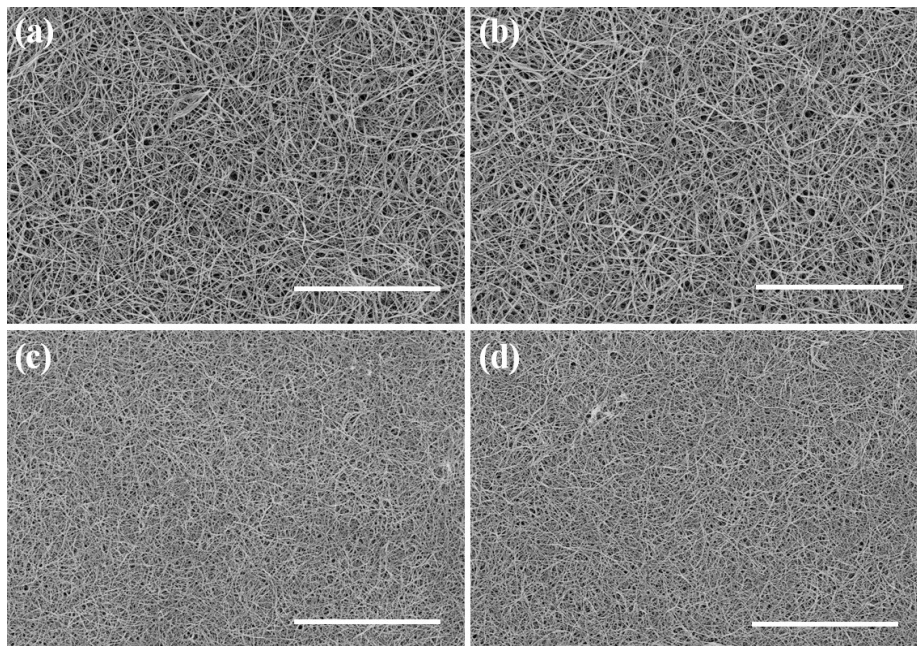


Figure S7. (a–d) FE-SEM images of $W_{18}O_{49}NW$ EC layers after 500 bending cycles at different positions. Scale bars: 4 μm (a, b); 8 μm (c, d).

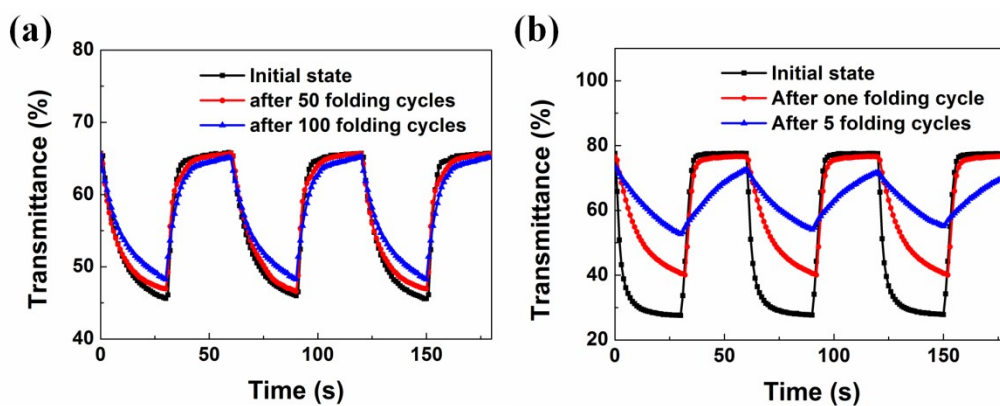
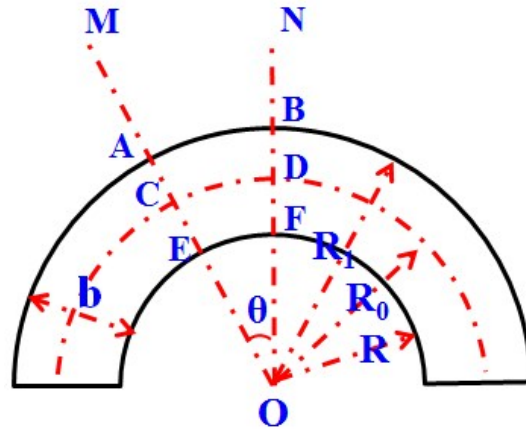


Figure S8. *In situ* transmittance responses (at 632.8 nm) of NEF-2 (a) and DEFs (b) between the colored and bleached states at different folding cycles.

Derivation of Equation (1) in the Manuscript:



Schematics for the materials under the bending condition.

As shown in the figure above, when the material is bent, the upper surface and lower surface of the material are subjected to the tensile and compressive stress, respectively. The material will be fractured if the deformation of upper surface reaches to the elongation at break (ΔL). Here, we assume that modulus of elasticity caused by the tensile and compressive stress is the same, and get the following derivation formulas.

$$\begin{aligned} \frac{(2\pi R_1 - 2\pi R_0) \times \frac{\theta}{360^\circ}}{2\pi R_0 \times \frac{\theta}{360^\circ}} &\leq \Delta L \\ \Rightarrow \frac{R_1}{R_0} &\leq \Delta L + 1 \\ \Rightarrow \frac{R + b}{R + b/2} &\leq \Delta L + 1 \\ \Rightarrow R &\geq \frac{b}{2} \left(\frac{1}{\Delta L} - 1 \right) \\ \Rightarrow R_{min} &= \frac{b}{2} \left(\frac{1}{\Delta L} - 1 \right) \end{aligned}$$

For inorganic materials, the elongation at break is very small. Therefore, the main way to improve the flexibility is to reduce the diameter or thickness of the inorganic material.

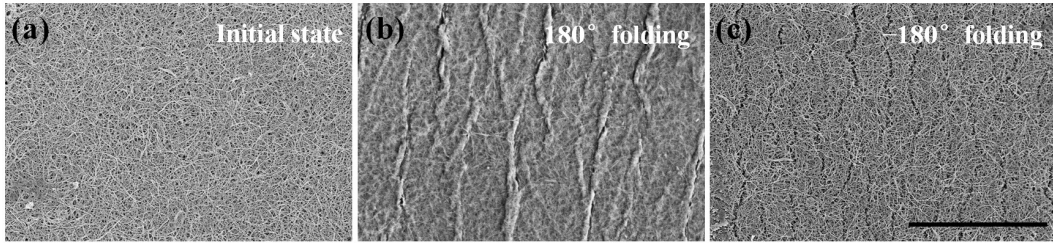


Figure S9. FE-SEM images of NEFs in initial state (a), after 50 folding cycles of 180° (b) and -180° (c). Scale bars: $10\ \mu\text{m}$.

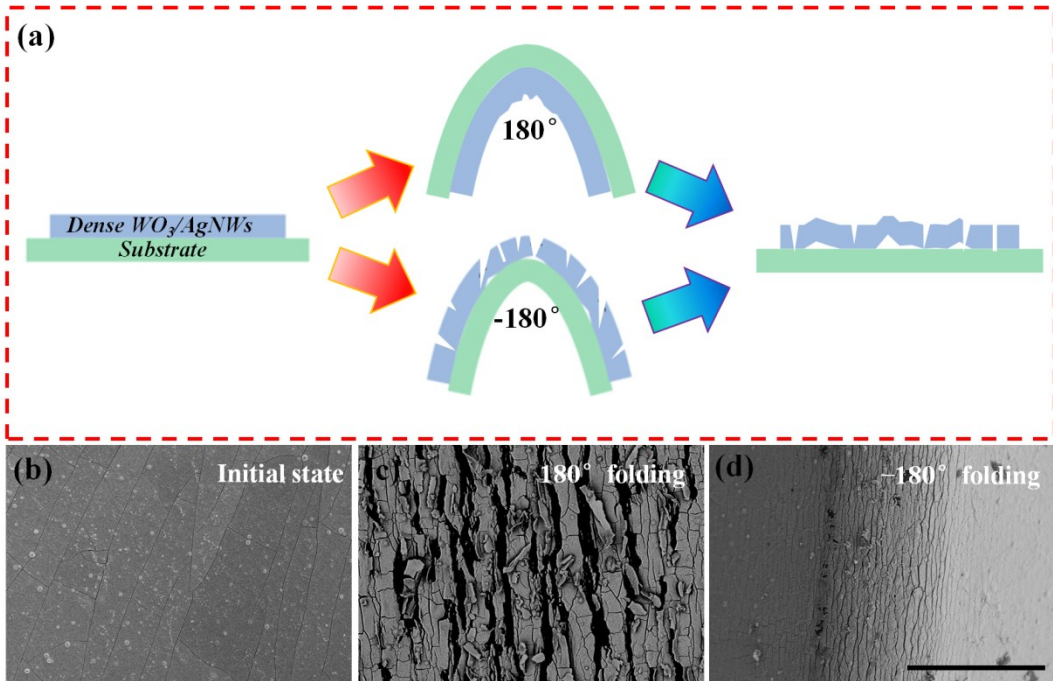


Figure S10. (a) Schematics for the mechanism of performance degradation of DEFs during the folding process; FE-SEM images of DEFs in initial state (b), after 50 folding cycles of 180° (c) and -180° (d). Scale bars: $50\ \mu\text{m}$.

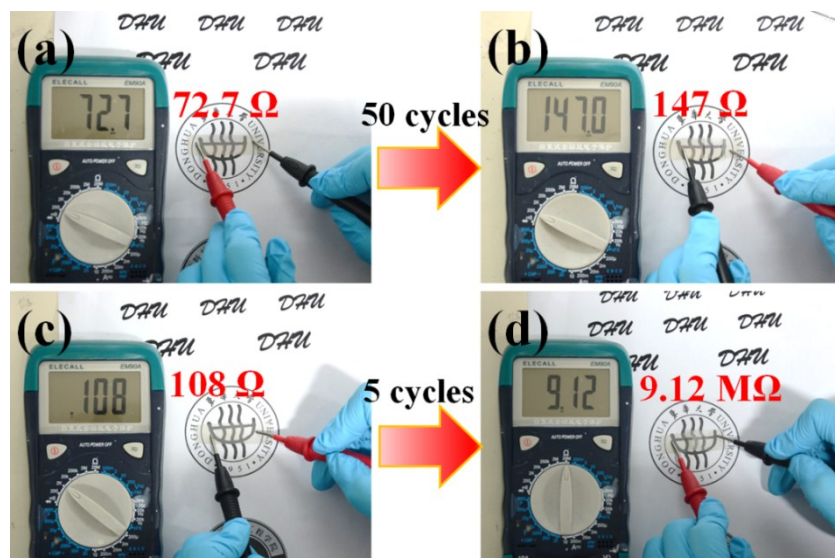


Figure S11. The surface resistance of NEFs before and after 50 folding cycles (a, b) and DEFs before and after 5 folding cycles(c, d).

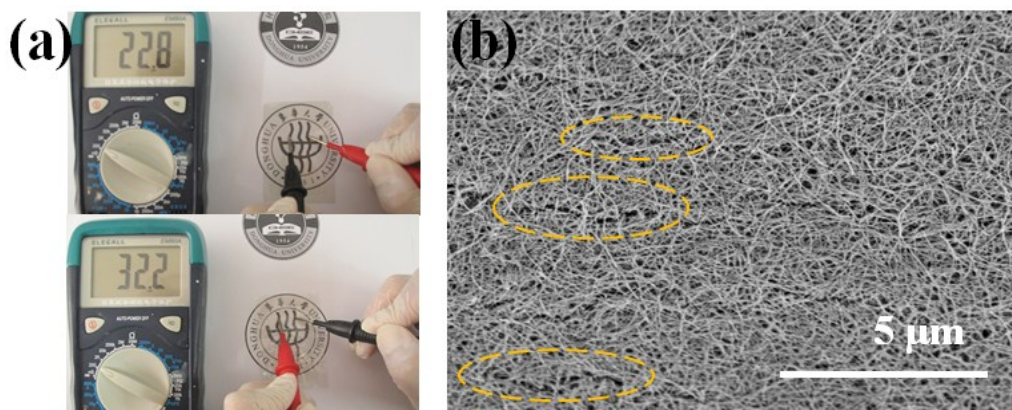


Figure S12. (a) The resistance changes in the area of conductive AgNW networks before (up) and after (down) crushing the EC films; (b) FE-SEM image of EC $W_{18}O_{49}NW$ networks at the crease after crushing the EC films.